ELSEVIER

Journal of Nuclear Materials 302 (2002) 1–8

journal of nuclear materials

www.elsevier.com/locate/jnucmat

Experimental investigation of the Zr corner of the ternary Zr–Nb–Fe phase diagram

M.S. Granovsky [a,b,*], M. Canay [b], E. Lena [b], D. Arias [a,b]

[a] *Departamento de Materiales, C.A.C. – Comisión Nacional de Energía Atómica, Av. del Libertador 8250, 1429 Buenos Aires, Argentina*

[b] *Instituto de Tecnología J. Sábato, CNEA-UNSAM, Av. del Libertador 8250, 1429 Buenos Aires, Argentina*

Received 24 October 2001; accepted 2 January 2002

Abstract

Intermediate phases in the Zr-rich region of the Zr–Nb–Fe system have been investigated by X-ray diffraction, optical and electron microscopy and electron microprobe analysis. The chemical composition ranges covered by the alloys studied here are: (41–97) at.% Zr, (32–0.9) at.% Nb and (0.6–38) at.% Fe. The phases found in this region were: the solid solutions α-Zr and β-Zr, the intermetallic Zr_3Fe with less than 0.2 at.% Nb in solution, two new ternary intermetallic compounds $(Zr + Nb)_2Fe$ 'λ_1' with a cubic Ti_2Ni-type structure in the composition range (2.4–13) at.% Nb and (31–33) at.% Fe, and $(Fe + Nb)_2Zr$ 'λ_2' indexed as hexagonal Laves phase $MgZn_2$ type (C14) with a wide range of compositions close to (35–37) at.% Zr, (12–31) at.% Nb and (32–53) at.% Fe.

PACS: 81.30.Bx

1. Introduction

Some zirconium alloys (Zry-2, Zry-4 or Zr–2.5% Nb) are generally used as cladding and structural materials in light and heavy water nuclear reactors due to their excellent neutron economy and corrosion resistance. On the other hand, multicomponent zirconium alloys with Sn, Nb and Fe are promising structural materials present in the active zone of nuclear reactors [1,2]. In these alloys several intermetallic precipitates [3–5] were identified, among them, the $Zr(NbFe)_2$ hexagonal close packed precipitate with $a = 0.54$ nm, $c = 0.88$ nm and $c/a = 1.63$ and composition: Zr = 37.5 at.%, Nb = 37.5 at.% and Fe = 25 at.%, measured in 1990 by Woo and Carpenter [3].

Only a few papers about phase diagrams of the Zr–Nb–Fe system were reported. Alekseeva and Korotkova worked in this system in the 1600–850 °C [6] and 800–500 °C [7] temperature ranges. They drew isothermal sections of the Zr–Nb–Fe diagram at several temperatures and identified a ternary chemical compound of composition: Zr-(8–10) at.% Nb-(36–38) at.% Fe which they called *T*; its crystal structure was not resolved.

In 1992 a critical assessment of the Zr–Nb–Fe phase diagram was reported [8], which was principally based upon [6,7].

Four intermediate phases are shown in the binary system Zr–Fe, assessed by Arias et al. [9], namely:

- Zr_3Fe, an orthorhombic BRe_3-type structure, stable up to 913 °C of the peritectoid reaction $\beta\text{-}Zr + Zr_2Fe \leftrightarrow Zr_3Fe$, the composition range is 24.0–26.8 at.% Fe,
- Zr_2Fe, a bct, Al_2Cu-type structure, with a temperature range of stability from the temperature of the eutectoid reaction $Zr_2Fe \leftrightarrow Zr_3Fe + ZrFe_2$ (about

* Corresponding author. Tel.: +54-11 6772 7382; fax: +54-11 6772 7362.

E-mail address: granovsk@cnea.gov.ar (M.S. Granovsky).

0022-3115/02/$ - see front matter
PII: S0022-3115(02)00718-3

775 °C) to 974 °C, temperature at which the peritectic reaction $L + ZrFe_2 \leftrightarrow Zr_2Fe$ takes place, and exists between 31.0 and 33.3 at.% Fe,

- $ZrFe_2$, a cubic Laves phase (C15) structure, composition ranges from 66.0 to 72.9 at.% Fe and a congruent melting point at 1673 °C and
- Zr_6Fe_{23}, a cubic Th_6Mn_{23}-type structure, which is practically a line compound, stable up to the temperature 1482 °C of the peritectic reaction $ZrFe_2 + L \leftrightarrow Zr_6Fe_{23}$.

The Nb–Zr phase diagram was assessed by Abriata and Bolcich [10] and Okamoto [11]. There are no intermediate phases in this system. The bcc β-Nb and β-Zr form a continuous solid solution at high temperature with a solid miscibility gap below 988 °C and a monotectoid reaction $\beta\text{-Zr} \leftrightarrow \alpha\text{-Zr} + \beta\text{-Nb}$ at 620 °C.

The Nb–Fe phase diagram was assessed by Okamoto [12]. Two intermediate phases are shown: the hexagonal Laves phase (C14), 'ε-Fe_2Nb', with a composition range from 32 to 37 at.% Nb and a congruent melting point at 1673 °C and the hexagonal Fe_7W_6-type 'μ-FeNb' which forms peritectically at $T = 1520$ °C following the reaction $\varepsilon\text{-}Fe_2Nb + L \rightarrow \mu\text{-FeNb}$, in the composition range 48–52 at.% Nb.

The aim of this work is to study the phases present in the Zr-rich region of the Zr–Nb–Fe system in the isothermal sections at 800 and 900 °C. These sections are based upon the experimental investigations on long-term heat treated samples, using optical and electron microscopy, X-ray diffraction and electron microanalysis.

2. Experimental details

Eight ingots (~12 g) were prepared in an arc furnace with a W electrode and a water-cooled copper crucible, in a high purity argon atmosphere (99.9995+). The starting materials were 99.9 wt% pure Fe and Nb, Zr and Zr–20% Nb with 0.1 wt% O and 0.08 wt% Fe. The ingots were melted and remelted at least four times in order to ensure homogeneity. The zirconium, niobium and iron contents of the alloys are given in Table 1.

Prior to heat treatment, the specimens were ground on silicon carbide papers and polished with diamond paste, carefully rinsed (hot ether), wrapped in clean tantalum foil and sealed in clean silica glass tubes in a high purity argon atmosphere. The furnace temperature control was ±3 °C.

Samples M-1 to M-7 were heat treated for 1200 h at 800 °C and for 500 h at 900 °C, the sample M-8 was heat treated at 900 °C for 500 h; the samples M-4 to M-7 were not heat treated at 900 °C because, according to [6,7] we expected the presence of liquid phases. After the heat treatments, silica glass tubes were quenched into cold water (without tube breaking) with a cooling rate $v_c \sim 30$ °C/s [13].

X-ray diffraction measurements on powdered specimens were performed with Cu K_α radiation at room temperature before and after the heat treatments, in a Phillips PW3HO X-ray diffractometer.

Prior to optical and electron microscopy and electron microanalysis, the samples were ground on silicon carbide paper, polished with diamond paste (7 and 1 μm) and etched with a solution of lactic acid, HF and HNO_3 at volume ratio 92:5:3. The sample M-1 was etched using a mixture of distilled water, HNO_3 and HF at volume ratio 50:45:5.

The composition of each phase was determined by wavelength dispersive electron-probe analysis with a Cameca S.X.50 electron-microprobe operated at 20 kV with an electron beam current of 50 nA and a chamber vacuum of 2×10^{-4} Pa. High purity metal standards, 99.99% Zr, Nb and Fe were used.

3. Results and discussion

3.1. Isothermal section at 800 °C

The isothermal section at 800 °C, which is presented in Fig. 1, has been mainly established using the results described in Table 2. Some of the results from the as-cast specimens (Table 3) were also taken into account as well as the results related to the Zr_2Fe and the $(ZrNb)Fe_2$ Laves phase reported by Ramos et al. [14], Mainardi et al. [15] and Kanematsu [16], respectively. Figs. 2(a) and (b) show two enlarged Zr rich regions, on which different phase fields are tentatively drawn in more detail.

The β-Zr X-ray and composition measurements reported in both Tables 2 and 3, correspond to the high temperature bcc phase retained at room temperature and are in keeping with the measured β-Zr phase preserved at room temperature in Zr–Nb alloys with contents higher than 8 at.% Nb [17,18].

Table 1
Nominal composition (at.%)

Sample	M-1	M-2	M-3	M-4	M-5	M-6	M-7	M-8
Zr	97.0	89.5	87.8	68.3	65.0	62.0	52.0	41.0
Nb	2.4	0.9	2.2	1.7	10.0	14.0	10.0	32.0
Fe	0.6	9.6	10.0	30.0	25.0	24.0	38.0	27.0

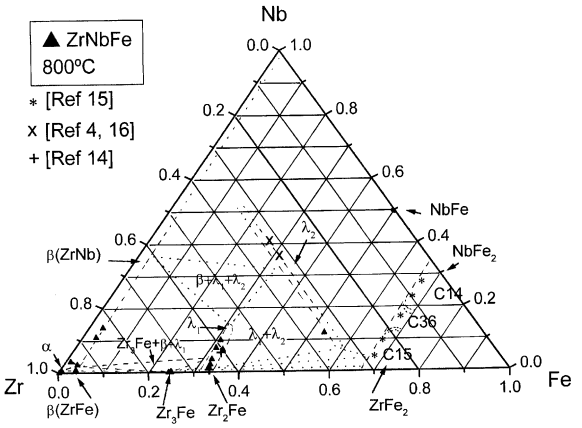

Fig. 1. Isothermal section at 800 °C (---- probable, ····· predicted).

The micrograph of the M-1 alloy (Fig. 3) shows the typical $(\alpha + \beta)$ Zr rich alloys structure, where the transformed β^T-Zr hexagonal close packed phase corresponds to a Widmanstätten-type transformation (diffusion assisted) which proceeds during cooling from the stable β-Zr phase temperature to room temperature.

In samples with more than 10 at.% Fe (M-3 through M-7) a new phase with cubic Ti_2Ni type structure was identified in the composition range Zr-(2.4–14.8) at.% Nb-(30–33) at.% Fe, $(ZrNb)Fe_2$, which we are calling λ_1 from now on.

The possible $(\alpha\text{-Zr} + \beta\text{-Zr} + Zr_3Fe)$ and the $(\alpha\text{-Zr} + \beta\text{-Zr} + \lambda_1)$ three phase regions were drawn taking into account the experimental results from M-2 and M-3 alloys. In Figs. 4(a) and (b) we can observe different Fe contents in the α-Zr, β-Zr and Zr_3Fe phases. These results and the measured chemical compositions corresponding to these phases (Table 2) allow us to delineate in this part of the diagram, two β phase regions, which correspond to the Zr–Nb and the Zr–Fe binary systems (Fig. 2(a)).

Chemical composition and the X-ray results measured in the samples M-4, M-5 and M-6, illustrate the two phase fields $(Zr_3Fe + \lambda_1)$ and $(\beta\text{-Zr} + \lambda_1)$, respectively. Fig. 5 shows the $(Zr_3Fe + \lambda_1)$ two phase field corresponding to the sample M-4.

The composition of sample M-7 was chosen close to the phase composition proposed by Alekseeva and Korotkova [6,7] in which they identified the T phase. Our experimental measurements show not one but two phases: the above mentioned cubic (Ti_2Ni)-type λ_1 phase and a new one we named λ_2, a hexagonal $MgZn_2$-type

Table 2
X-ray diffraction and electron microprobe results corresponding to Zr–Nb–Fe alloys, heat treated at 800 °C (1200 h)

Sample	Alloys (at.%)			Structure-X-ray diffraction			Composition (at.%)			Phases
	Zr	Nb	Fe	System	Prototype	Lattice parameter (nm)	Zr	Nb	Fe	
M-1	97.0	2.4	0.6	Hcp	Mg		98.9	<0.8	<0.3	α-Zr
				Hcp	Mg		95.5	3.4	1.1	β^T-Zr[a]
M-2	89.5	0.9	9.6	Hcp	Mg	$a = 0.325$ $c = 0.518$	99.8	0.0	<0.2	α-Zr
				Hcp	Mg		95.8	0.9	3.4	β^T-Zr[a]
				Orthorhombic	BRe_3		75.6	0.0	24.4	Zr_3Fe
M-3	87.8	2.2	10	Hcp	Mg		94.5	2.5	3.0	β^T-Zr[a]
				Orthorhombic	BRe_3		75.0	0.2	24.8	Zr_3Fe
				Cubic	Ti_2Ni		64.0	4.0	32.0	$(ZrNb)_2Fe$-λ_1
M-4	68.3	1.7	30	Orthorhombic	BRe_3	$a = 0.329$ $b = 1.075$ $c = 0.887$	75.0	0.1	24.9	Zr_3Fe
				Cubic	Ti_2Ni		65.1	2.4	32.5	$(ZrNb)_2Fe$-λ_1
M-5	65.0	10	25	Bcc	W	$a = 0.355$	86.0	11.0	3.0	β-Zr
				Cubic	Ti_2Ni	$a = 1.216$	59.0	10.0	31.0	$(ZrNb)_2Fe$-λ_1
M-6	62	14	24	Bcc	W	$a = 0.354$	83.0	14.0	3.0	β-Zr
				Cubic	Ti_2Ni	$a = 1.219$	56.0	12.0	32.0	$(ZrNb)_2Fe$-λ_1
M-7	52	10	38	Cubic	Ti_2Ni	$a = 1.212$	60.0	7.0	33.0	$(ZrNb)_2Fe$-λ_1
				Hexagonal	$MgZn_2$		35.0	12.0	53.0	$Zr(NbFe)_2$-λ_2

[a] β^T-Zr composition, which corresponds to the β-Zr high temperature phase, measured in $[10 \times 10\ \mu m^2]$ areas.

Table 3
X-ray diffraction and electron microprobe results corresponding to the as-cast Zr–Nb–Fe alloys

Sample	Alloys (at.%)			Structure-X-ray diffraction			Composition (at.%)			Phases
	Zr	Nb	Fe	System	Prototype	Lattice parameter (nm)	Zr	Nb	Fe	
M-2	89.5	0.9	9.6	Hcp	Mg	$a = 0.324$ $c = 0.516$	93.0	0.8	6.2	β^T-Zr[a]
				Orthorhombic	BRe_3	$a = 0.332$ $b = 1.177$ $c = 0.898$	72.5	0.5	27.0	Zr_3Fe
M-3	87.8	2.5	10.0	Hcp	Mg		93.0	2.3	4.7	β^T-Zr[a]
				Orthorhombic	BRe_3	$a = 0.334$ $b = 1.079$ $c = 0.926$	72.5	1.7	25.8	Zr_3Fe
M-4	68.3	1.7	30.0	Tetragonal	Al_2Cu	$a = 0.644$ $c = 0.528$	73.5	0.5	26.0	Zr_2Fe
				Cubic	Ti_2Ni	a = 1.218	65.9	1.7	32.4	$(ZrNb)_2Fe$-λ_1
M-5	65.0	10.0	25.0	Bcc	W	a = 0.352	72.2	13.7	9.1	β-Zr
				Cubic	Ti_2Ni	$a = 1.218$	63.2	7.7	29.1	$(ZrNb)_2Fe$-λ_1
M-7	52.0	10.0	38.0	Cubic	Ti_2Ni	$a = 1.217$	61.2	7.6	31.2	$(ZrNb)_2Fe$-λ_1
				Orthorhombic	BRe_3	$a = 0.334$ $b = 1.054$ $c = 0.892$				Zr_3Fe
				Hexagonal	$MgZn_2$		41.0	12.2	46.87	$Zr(NbFe)_2$-λ_2

[a] β^T-Zr, the same meaning as in Table 2.

Laves phase (C14) structure and the composition range Zr-(12–31) at.% Nb-(31.7–50) at.% Fe, $Zr(NbFe)_2$, Fig. 6 illustrates both phases. The experimental results in the M-7 as-cast sample, Table 3, indicate the presence of λ_1 and λ_2 plus the Zr_3Fe intermetallic.

3.2. Isothermal section at 900 °C

In samples M-5, M-6 and M-7 we identified phases with practically identical composition and X-ray diffraction results as the samples heat treated at 800 °C. The micrograph of the M-7 alloy shows the λ_1 and λ_2 phases. (Fig. 7(a)) and the corresponding as-cast sample (Fig. 7(b)) illustrates the λ_1 and λ_2 plus the Zr_3Fe phases.

The sample M-8, whose chemical composition was selected close to the composition of the precipitates identified in the Zr multicomponent alloy Zr–1Sn–1Nb–0.1(0.4)Fe–0.1O [3–5], showed three phases, β-Zr Nb + $\lambda_1 + \lambda_2$.

The 900 °C isothermal section presented in Fig. 8, has been drawn using the experimental results reported in Table 4. We also used some experimental results measured by other authors: the cubic and hexagonal $(ZrNb)Fe_2$ Laves phase [16], the reported tetragonal and cubic $(ZrNb)_2Fe$ [14,15], and some intermetallic precipitates composition [3,17].

3.3. Discussion

Several phases were identified at different compositions of the Zr-rich region:

α-Zr: has a hcp structure with very low Nb and Fe in solution.

β^T-Zr: has a hcp structure with ≅3 at.% Fe and Nb, which corresponds to a Widmanstätten-type transformation when cooling from β-Zr-regions.

β-Zr: has a bcc structure at room temperature retained after quenching [18,19] with ≅3 at.% Fe and ≅36 at.% Nb. These results together with the solubility of Fe in the binary Nb–Fe system indicate that the β-ZrNb accepts ≅3 at.% Fe in solid solution.

Zr_3Fe: has an orthorhombic structure, practically stoichiometric with the maximum solubility of Nb less than 0.2 at.%.

$(ZrNb)_2Fe$: 'λ_1' identified as a cubic Ti_2Ni type structure with a lattice parameter between $a = 1.212$ nm and $a = 1.219$ nm in the composition range Zr-(2.4–14.8) at.% Nb-(30–33) at.% Fe. At this point it is important to recall that the Ti_2Ni structure was detected and thoroughly studied in several ternary alloy systems of the IV A transition metals Zr, Hf or Ti with either two (second or third) transition metals or with such a metal and oxygen, as reported in [20–23].

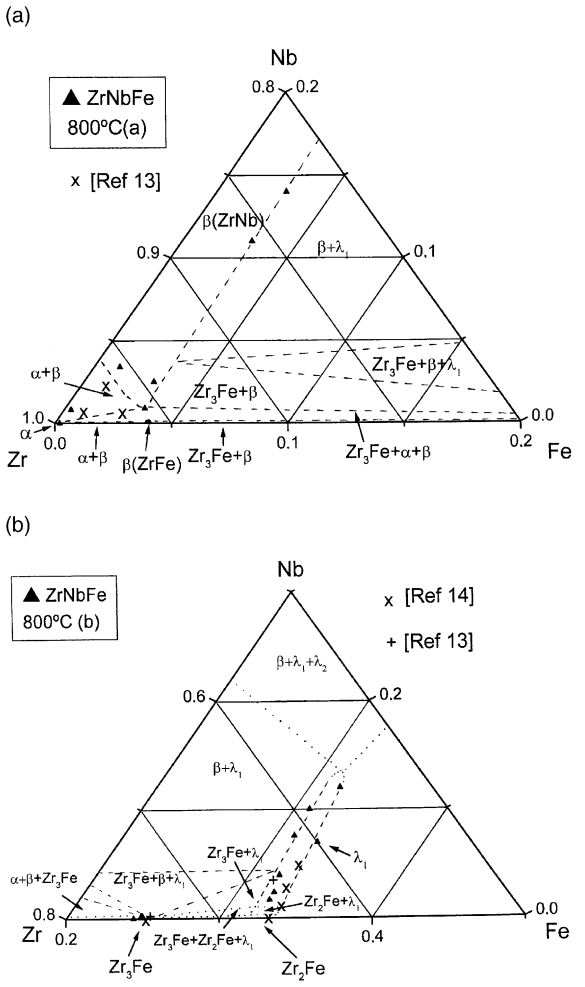

Fig. 2. (a) and (b), enlarged Zr rich regions corresponding to the isothermal section at 800 °C (---- probable, ····· predicted).

$Zr(NbFe)_2$: 'λ_2' indexed as hexagonal Laves phase $MgZn_2$ type (C14), in the composition range Zr-(12–31) at.% Nb-(31.7–50) at.% Fe, with lattice parameters $a = 0.5327$ nm, $c = 0.8630$ nm. This 'λ_2' Laves phase is located in the central part of the diagram in a different region from that of the well-known Laves phase $(ZrNb)Fe_2$. With the help of the structural AB_2 Pettifor map [24,25], the stability of both Laves phases was verified. The Zr–Fe–Mo system shows in a qualitative way the same situation, the coexistence of Laves phases both in the Fe-rich corner and in the middle of the diagram.

Alekseeva and Korotkova [6,7] reported the X-ray diffraction results corresponding to the 'T' phase alloy but a new reinterpretation of these results clearly indicates that their samples were in a two phase field ($\lambda_1 + \lambda_2$).

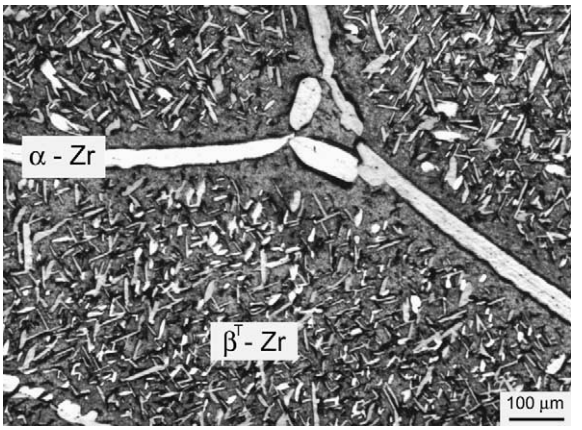

Fig. 3. Optical micrograph corresponding to the M-1 alloy, isothermal annealing temperature at 800 °C (1200 h). High temperature α-Zr plates + β-Zr regions transformed into α-Widmanstätten during the cooling from 800 °C to room temperature (β^T-Zr).

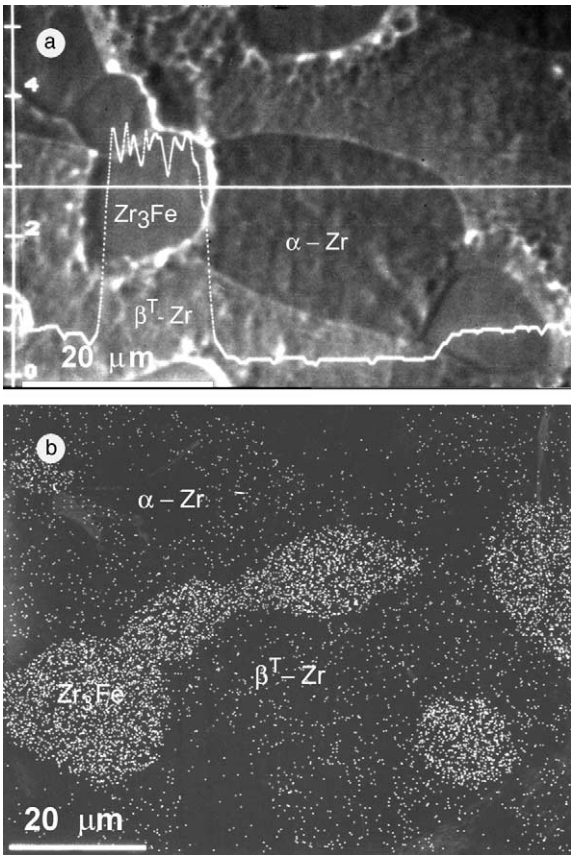

Fig. 4. Sample M-2 heat treated at 800 °C (1200 h): (a) backscattered electron micrograph and the variation of the Fe lineal section of the sample; (b) X-ray Fe mapping.

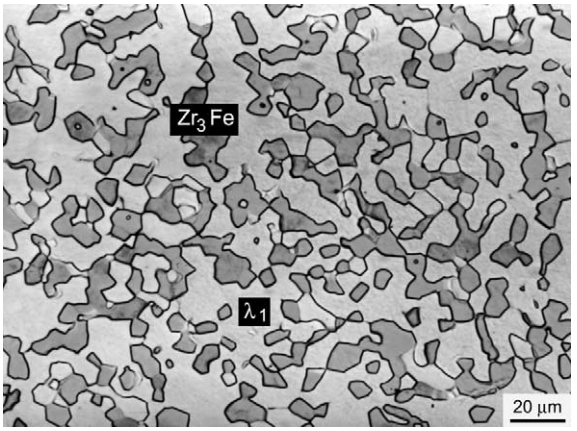

Fig. 5. Optical micrograph of the M-4 alloy heat treated at 800 °C (1200 h). Isothermal ($Zr_3Fe + \lambda_1$) structure.

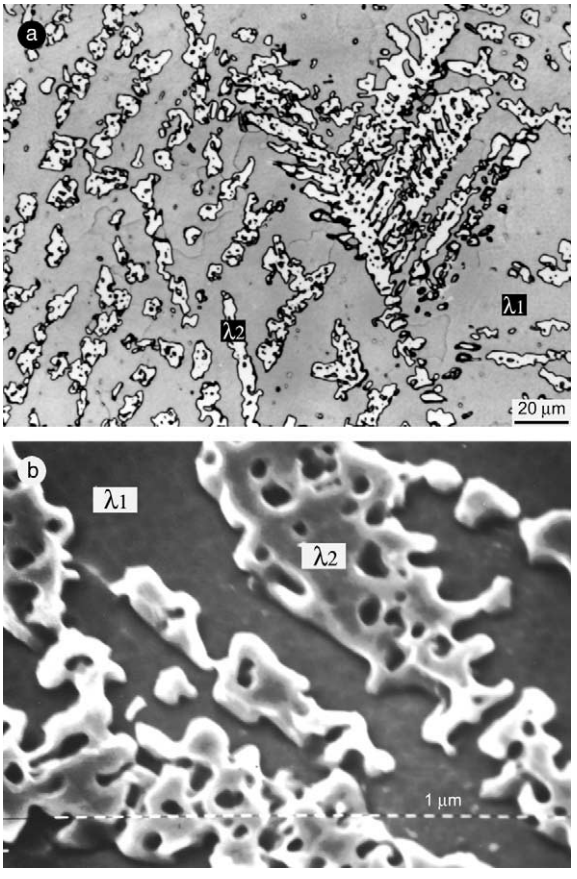

Fig. 6. Sample M-7 heat treated at 800 °C (1200 h): (a) optical micrograph; (b) scanning electron micrograph. Isothermal ($\lambda_1 + \lambda_2$) structure.

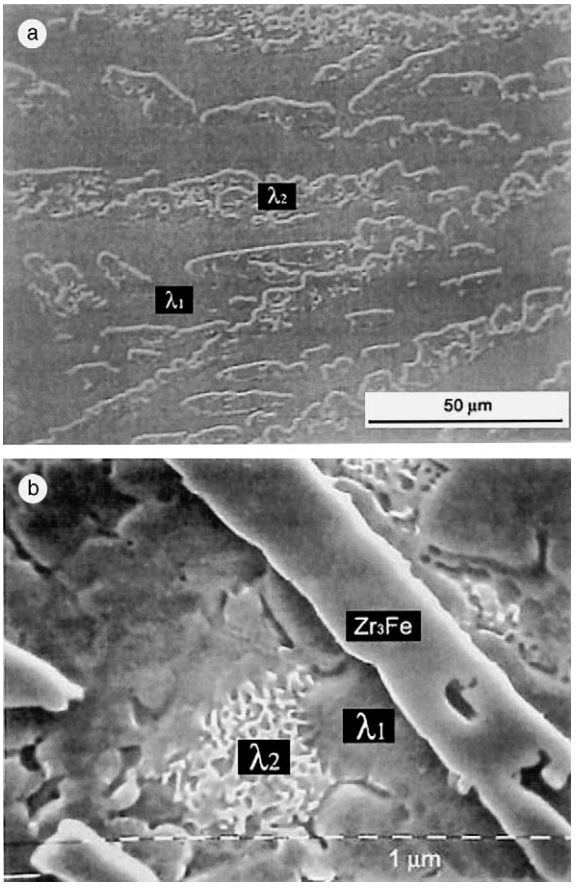

Fig. 7. Scanning electron micrograph of the M-7 alloy: (a) isothermal annealing at 900 °C (500 h), ($\lambda_1 + \lambda_2$) structure; (b) ($\lambda_1 + \lambda_2 + Zr_3Fe$) structure in the as-cast sample.

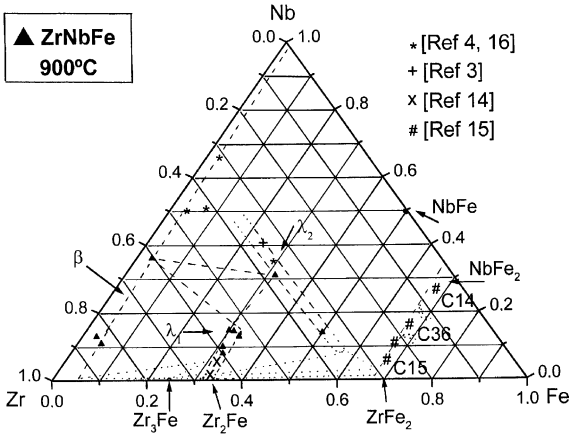

Fig. 8. Isothermal section at 900 °C (---- probable, ····· predicted).

Table 4
X-ray diffraction and electron microprobe results corresponding to Zr–Nb–Fe alloys, heat treated at 900 °C (500 h)

Sample	Alloys (at.%)			Structure-X-ray diffraction			Composition (at.%)			Phases
	Zr	Nb	Fe	System	Prototype	Lattice parameter (nm)	Zr	Nb	Fe	
M-5	65.0	10.0	25.0	Bcc	W	$a = 0.354$	84.0	11.0	5.0	β-Zr
				Cubic	Ti_2Ni	$a = 1.216$	59.0	10.0	31.0	$(ZrNb)_2Fe$-λ_1
M-6	62.0	14.0	24.0	Bcc	W	$a = 0.354$	84.0	13.0	3.0	β-Zr
				Cubic	Ti_2Ni	$a = 1.218$	54.0	13.0	33.0	$(ZrNb)_2Fe$-λ_1
M-7	52.0	10.0	38.0	Cubic	Ti_2Ni	$a = 1.212$	60.0	8.0	32.0	Ti_2Ni
				Hexagonal	$MgZn_2$		36.0	14.0	50.0	$Zr(NbFe)_2$-λ_2
M-8	41.0	32.0	27.0	Bcc	W		60.6	36.2	3.2	β-ZrNb
				Cubic	Ti_2Ni		55.2	14.8	31.7	$(ZrNb)_2Fe$-λ_1
				Hexagonal	$MgZn_2$	$a = 0.5327$ $c = 0.8630$	37.3	31.0	31.7	$Zr(NbFe)_2$-λ_2

4. Conclusions

The Zr rich corner of the Zr–Nb–Fe system has been investigated by optical and electron microscopy, X-ray diffraction and electron microprobe analysis on quenched and heat treated samples. Equilibrium phase relations at 800 and 900 °C were established.

Two ternary compounds, $(Zr + Nb)_2Fe$ 'λ_1' identified as a cubic Ti_2Ni type and $(Fe + Nb)_2Zr$ 'λ_2' hexagonal Laves phase type $MgZn_2$ have been found, and their chemical compositions were measured.

Binary and ternary regions of the diagrams at 800 and 900 °C were proposed. However, some of them are drawn as 'probable' and some others as 'predicted'.

Taking into account the experimental results and the solubility in the β-phase of the Nb in the Zr–Nb system and the Fe in the Nb–Fe system at 900 °C we suggest the bcc solid solution region in the Zr–Nb–Fe system.

Acknowledgements

The authors are specially indepted to Dr M. Ortiz Albuixech for her help in the X-ray diffraction analysis and Mr R. Castillo Guerra for his help in the micrographs. This work was supported by CNEA and CONICET-Argentina (Grant PIP No. 4040/96).

References

[1] V.A. Markelov, V.Z. Rafikov, S.A. Nikulin, V.I. Goncharov, V.N. Shishov, A.Yu. Gusev, E.K. Chesnokov, Phys. Metals Metall. 77 (1994) 380.
[2] G.P. Sabol, G.R. Kilp, M.G. Balfour, E. Roberts, in: Proceedings of the 8th International Symposium on Zirconium in the Nuclear Industry, ASTM STP, 1023, 1989, p. 227.
[3] O.T. Woo, G.J.C. Carpenter, in: 741 Proceedings of the XIIth International Congress for Electron Microscopy, AECL Report, 10264, 1990, p. 132.
[4] A.V. Nikulina, V.A. Markelov, M.M. Peregud, V.N. Voevodin, V.L. Panchenko, G.P. Kobylyansky, J. Nucl. Mater. 238 (1996) 205.
[5] G.P. Sabol, R.A. Comstock, P. Larouere, R.N. Stanutz, in: Proceedings of the 10th International Symposium on Zirconium in the Nuclear Industry, ASTM STP, 1245, 1994, p. 724.
[6] Z.M. Alekseeva, N.V. Korotkova, Inv. Akad. Nauk SSSR, Metally 1 (1989) 199.
[7] N.V. Korotkova, Z.M. Alekseeva, Inv. Akad. Nauk SSSR, Metally 3 (1989) 207.
[8] V. Raghavan (Ed.), Phase Diagrams of Ternary Fe Alloys, part 6b, vol. 248, Indian Institute of Metals, Calcutta, 1992, p. 1031.
[9] D. Arias, M.S. Granovsky, J.P. Abriata, in: H. Okamoto (Ed.), Phase Diagrams of Binary Iron Alloys, ASM International, Materials Park, OH, 1993, p. 467.
[10] J.P. Abriata, J.C. Bolcich, Bull. Alloy Phase Diagrams 3 (1982) 34.
[11] H. Okamoto, J. Phase Equilibria 13 (1992) 576.
[12] H. Okamoto, J. Phase Equilibria 16 (1995) 369.
[13] M. Ruch, D. Arias, Scripta Met. Mater. 24 (1990) 1577.
[14] C. Ramos, C. Saragovi, M. Granovsky, D. Arias, Hyperfine Interact. 122 (1999) 201.
[15] D.S. Mainardi, D. Arias, M.S. Granovsky, XXVI Reunión Anual de la Asociación Argentina de Tecnología Nuclear, Bariloche Argentina, 1999.
[16] Z. Kanematsu, J. Phys. Soc. Japan 27 (4) (1969) 849.
[17] A.V. Nikulina, V.N. Shishov, M.M. Peregud, A.V. Tselischev, V.K. Shamardin, G.P. Kobylyansky, in: Proceedings of the 18th International Symposium on Effects of Radiation on Materials, ASTM-STP, 1261, 1999, p. 1045.
[18] P. van Effenterre, G. Cizeron, P. Lacombe, J. Nucl. Mater. 31 (1969) 269.
[19] G.J. Cuello, A. Fernandez Guillermet, G.B. Grad, R.E. Mayer, J.R. Granada, J. Nucl. Mater. 218 (1995) 236.

[20] M.V. Nevitt, J.W. Downey, R.A. Morris, Trans. Metall. Soc. AIME 218 (1960) 1019.
[21] F. Aubertin, U. Gonser, S.J. Campbell, H.G.Z. Wagneer, Z. Metallkd. 76 (1985) 237.
[22] I.Yu. Zavaliy, J. Alloys Compd. 291 (1999) 102.
[23] I.Yu. Zavaliy, A.B. Riabov, V.A. Yartys, G. Wiesinger, H. Michor, G. Hilscher, J. Alloys Compd. 265 (1998) 6.
[24] D.G. Pettifor, Solid State Commun. 51 (1984) 31.
[25] D.G. Pettifor, Mater. Sci. Technol. 4 (1988) 675.